Unified Current-Programmed Digital Controller for Non-Inverting Buck-Boost Converter with Optimal Steady-State and Transient Conditions

Tom Urkin, *Student Member*, *IEEE* and Mor Mordechai Peretz, *Member*, *IEEE*
The Center for Power Electronics and Mixed-Signal IC, Department of Electrical and Computer Engineering
Ben-Gurion University of the Negev, P.O. Box 653, Beer-Sheva, 8410501 Israel
tomur@post.bgu.ac.il, morp@bgu.ac.il
http://www.ee.bgu.ac.il/~pemic

***Abstract* – This paper introduces a new current-programmed controller for non-inverting buck-boost converters. The controller facilitates tight voltage regulation and excellent transient convergence, all carried out through a simple CPM controller hardware. Steady-state operation for the full range of conversion ratios is supported with seamless transitions between modes and improved efficiency and ripple characteristics around unity conversion gain. In case of a load transient, an optimized boundary control scheme achieves near-optimal recovery, with programmable constrains for the voltage deviation and inductor current, covering the entire range of conversion ratios. The operation of the controller is experimentally verified on a 2-15V input to 3.3V output, non-inverting buck-boost converter, demonstrating significant improvement in steady-state around unity gain as well as fast convergence for load transients with programmable constraints for the output voltage deviation and inductor current.**

Keywords – Digital control, state-space control, non-inverting buck-boost, efficient energy processing.

I. Introduction

Following the rapid growth in computing power and in particular for portable electronics, the specifications and restrictions on efficient usage of battery-powered applications have been significantly tighten to assure compact and light devices with long operation cycles. In variety of such applications, in particular as those prone to wide range of ambient temperature swing [1], or for cells with wide voltage range [2]-[5], the source voltage can be higher or lower than the target regulated output. Another case that requires front-end conversion flexibility is for high-performance programmable-gate arrays (PGAs) that may be fed by multiple sources [6].

It is apparent that a flexible SMPS capable of stepping down, up, or operating around unity is essential. In addition, since direct conversion as point-of-load is preferred due to efficiency considerations, then the SMPS is also required to satisfy transient requirements and comply with the system dynamic characteristics [7]-[9]. Non-Inverting Buck-Boost (NIBB) converter configuration has a long track-record of carrying out the above-mentioned prerequisites. Although it comprises of four switches with two devices in the conduction path, its efficiency characteristics and ripple efforts have demonstrated superiority in comparison to a conventional buck-boost arrangement. One of the more attractive features of NIBB converters is the capability of operating as a buck converter when step-down operation is needed and as a boost for step-up. Remaining is the region around unity in which, apparently, this converter lacks advantages than its precursor. Fortunately, several fundamental studies in the recent years [9]-[11], have been conducted around the unity region and demonstrated ripple and efficiency enhanced modes of operations. A key challenge would be to embed all required features as well as superior transient capabilities in a simple and unified controller.

Load transient recovery is a critical factor in the design of modern switch-mode power supplies. In particular, sizing of the passive components predominantly depends on the recovery pattern of the system, since largest deviations occur during transient events. To reduce the requirements of the converter's passives and as a result, the overall volume of the SMPS, high-performance voltage regulators typically employ transient-oriented controllers, which can be either boundary or hybrid. Boundary controllers [12],[13] , among them hysteretic and sliding-mode controllers, are geometry-based methods that split the state-plane such that in one side of the boundary the

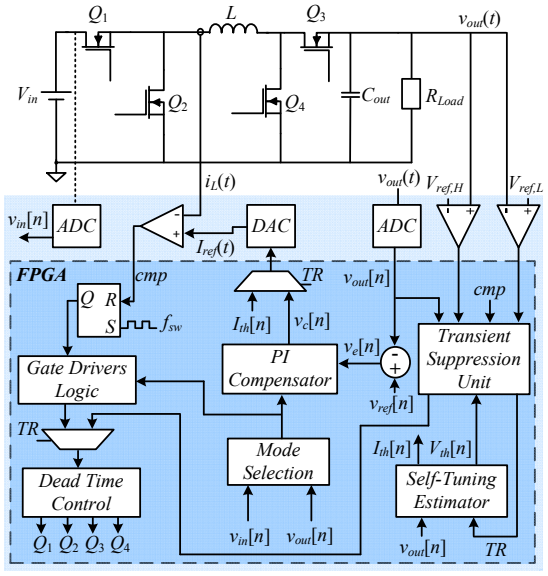

Fig. 1. Simplified schematic diagram of a non-inverting buck-boost converter with current-programmed controller.

operation is governed by the on state and by the off state at the other side of the boundary. Hybrid controllers [14],[15] switch between two or more control laws based on the system state variables in order to obtain the performance goals. Within the context of switch-mode applications, the hybrid control law typically incorporates a steady-state linear controller (i.e., PI or PID), to allow constant operating frequency, which simplifies the design of the power converter.

As opposed to buck-type conversion, which is classified as direct-energy transfer and characterized with closed-form optimal solution for the load transient recovery and deviation, in boost-type circuits general optimization of the recovery targets is significantly more complex. For example, time-optimal recovery of buck-boost converter results in extensive voltage drop, much larger than the minimum value that can be obtained [16]. However, ideal minimal voltage drop for boost-type conversion requires infinite convergence time. On the other hand, since in this study a NIBB converter configuration is used to support wide range of conversion ratios, it stands to reason that the recovery pattern may be further enhanced, beyond the conventional definition of time-optimality, benefiting from the topological flexibility of the converter. For instance, adding boosting phase to a loading step while in step-down conversion (buck mode in steady-state).

The objective of this study is to introduce a new controller architecture and implementation for NIBB converter as shown in Fig. 1. It employs a simple current-programmed configuration to realize a hybrid-type controller with tight voltage regulation and excellent transient convergence, all carried out through a classic two-loop controller hardware. The inner loop is a comparator-based peak (hysteretic) current mode, which receives information from an outer-loop digital voltage-mode compensation scheme. The new controller supports operation in steady-state for the full range of conversion ratios with seamless transition between modes and improved efficiency and ripple characteristics around unity gain, compared to the conventional control schemes for buck-boost converters. Load transients and mitigation of other large-signal deviations are supported by the same hardware of the steady-state controller, but with different control objectives. Near-optimal load transient recovery profile, with programmable constraints of the output voltage deviation and inductor current, are achieved for the entire conversion range in both loading and unloading conditions.

The rest of the paper is organized as follows: Section II describes the unified controller architecture and details its principle of operation. Section III covers the transient control scheme in the various regions of conversion modes. Practical implementation aspects are addressed in section IV. Experimental verification is provided in section V. Section VI concludes the paper.

II. Controller Architecture and Operation

The NIBB converter, shown in Fig. 1 has four switches, which can be divided into two pairs: Q_1 and Q_2 make up the buck pair while Q_3 and Q_4 make up the boost pair. The operation for each pair of switches is complementary. The control objective in this study is to sustain a regulated output voltage for any setting of the input voltage (within the design specifications), which may be above, below or equal to the target output, and significantly vary during operation. To this end, the system governor adjusts the switching sequence so that the converter operates at the best performing configuration for the specific voltage gain. By assignment of two duty ratio notations, d_{buck} for the pair of Q_1-Q_2 and d_{boost} for Q_3-Q_4, then the dc conversion ratio for NIBB converter can be uniformly expressed (i.e., regardless of information for the specific mode of operation) as [9]:

$$\frac{V_{out}}{V_{in}} = \frac{d_{buck}}{1-d_{boost}} . \quad (1)$$

In the following, the architecture and operation of the new controller are detailed. Emphasis is given to the challenges of the continuously varying input voltage and efficient regulation around unity conversion ratio.

A. Controller Architecture and Operation

As can be seen in Fig. 1, the controller follows a two-loop current-programmed configuration with a digital outer voltage loop and inner comparator-based current loop. The voltage loop produces a digital reference, $v_c[n]$ based on the error signal, $v_e[n]$, of the voltage loop for either the peak or valley current values, depending on the operation mode. The reference current values are converted to continuous-time representation by a digital-to-analog converter (DAC) which feeds the positive input of a comparator.

To ensure proper regulation of the output voltage for all conversion ratios, a state-machine algorithm described by the flowchart of Fig. 2, has been incorporated. The mode of operation (i.e., step-up, step-down or unity) is determined in this study by samples of the input voltage, $v_{in}[n]$ and output voltage, $v_{out}[n]$, which are the inputs to the mode selection block (see Fig. 1). To prevent toggling and to ensure smooth transition between modes, the assignment of the operation mode is determined based on the steady-state value for the output voltage, $v_{ref}[n]$, and in addition, a hysteresis band is assigned around unity conversion ratio.

Efficient way that exploits the flexibility of this converter is to operate in the dedicated converter topology that is suitable for the conversion ratio based on the status of the input and output voltages. In this way, rather than operating in buck-boost mode for the entire range, a buck setup is preferred for step-down conversion, whereas step-up conversion is to be performed with a boost arrangement. It has been established in [17],[18] that this approach improves the power conversion efficiency and reduces the components ripple. Still remaining however, is the region around unity conversion ratio where buck-boost operation prevails since neither buck nor boost converters can achieve pure unity conversion while regulating the output voltage. To this end, several approaches to lower the ripple efforts have been pursued in recent years[9],[17]. This study too adopts the approach of operating in an enhanced mode around unity conversion ratio, with some unique adjustments of the enhanced modes selection and realization. To cover all conversion modes and move between them seamlessly, the operation of the steady-state controller has been segmented into four. There are two conventional cases of buck and boost, and two new modes of enhanced-buck and

enhanced-boost, which are distinguished by the voltage status around the unity conversion ratio. The topology subcircuits for all operating modes are shown in Fig. 3 with typical current waveforms in Fig. 4.

For the case that $V_{in}>V_{out}$, the controller operates in a conventional buck mode. Here, Q_3 is kept on, Q_4 is off and the pair Q_1 and Q_2 toggles complementary. Voltage regulation is facilitated through valley current control, which determines the duty ratio of the toggling transistor pair. Equivalent subcircuits for this operation mode are shown in Fig. 3b-c with inductor current shown in Fig. 4a.

For the case that $V_{in}<V_{out}$, the controller operates in a conventional boost mode. The passive pair here is Q_1-Q_2 while Q_3-Q_4 switching complementary (Fig. 3a-b). To utilize the same control hardware without modification, peak current control now determines the duty ratio for output voltage regulation (see Fig. 4b).

The enhanced-buck mode is engaged where the input voltage is slightly higher than the output voltage. In this case, the conventional valley current control, employed for the pure buck mode, is modified to a three-phase sequence for a switching period, resulting in inductor current waveform as shown in Fig. 4c. In the first interval t_{e1}, Q_2 and Q_3 are on (subcircuit Fig. 3b) and the inductor current ramps down with a slope of $(-V_{out})/L$ to the valley value assigned by the current reference. The second interval t_{e2} is a short boosting phase (subcircuit Fig. 3a) where the inductor current ramps up with a slope of V_{in}/L. In the third interval t_{e3} (subcircuit Fig. 3c) the inductor current continues to ramp up, but with a moderate slope of $(V_{in}-V_{out})/L$, until the end of the cycle. The boosting phase timing can be realized by either assignment of a fixed duty ratio d_{boost} as employed in [9],[10], or as carried out in this study by changing the reference value to the comparator. Using the latter, cycle-by-cycle protection merit is maintained continuously along the entire range of conversion ratios.

Enhanced-boost mode is used for the case that the input voltage is slightly lower than the output voltage. In a similar way as the previous mode, a three-phase sequence is utilized, now with the difference that peak current value is initially

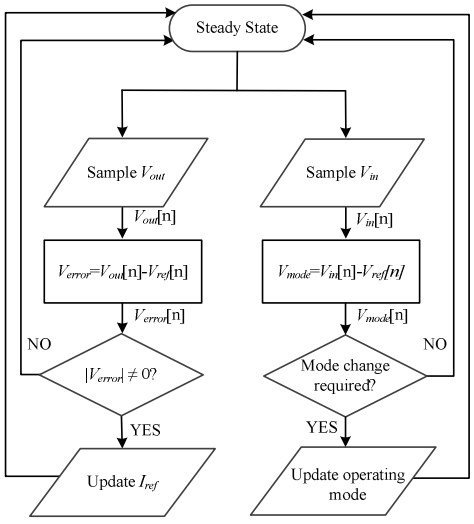

Fig. 2. Flowchart of the controller's operation in steady state.

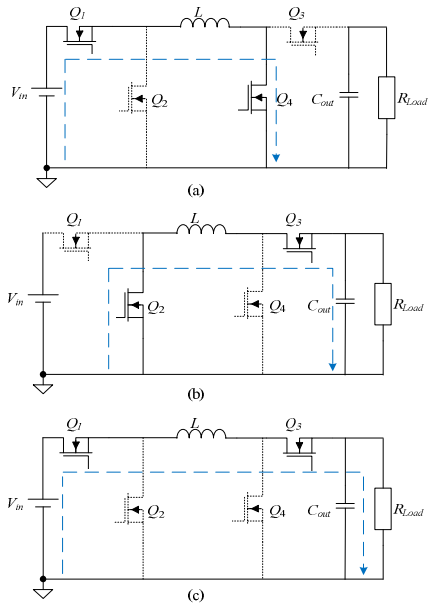

Fig. 3. Equivalent circuit of the non-inverting buck-boost converter in various stages of operation.

obtained. A typical inductor current waveform for this case is depicted in Fig. 4d. Here, in the first interval t_{e1}, the current ramps up with a slope of V_{in}/L (subcircuit Fig. 3a). Then, in t_{e2}, the inductor discharges onto the load with a slope of $(-V_{out})/L$. Finally, in t_{e3}, the inductor current ramps down in buck-mode with a moderate slope of $(V_{in}-V_{out})/L$. To facilitate the second phase, here too there are two options; One with a fixed duty ratio[9],[10] , now d_{buck}. The second alternative, which has been carried out in this study, is by the current comparator.

From the above description, it implies that a single-comparator current-mode architecture is sufficient to all four modes, covering the full range of conversion ratios with enhanced conversion efficiency and lower ripple effort around unity ratio. These are achieved while retaining cycle-by-cycle current protection and simplifying the voltage-loop compensator by reducing the system order, because of the tight current-programmed control [19],[20]. In addition, since information on both state variables is available to the controller, it enables to facilitate optimal load transient recovery by employing boundary or sliding-mode control law without hardware modification - this is addressed in the next section.

B. Impact of the Operation Mode on the Inductor's Current rms Value

Conduction losses are a primary contributor to the efficiency of buck-boost converters, in particular around unity conversion ratio. Since this study presents a modified operating sequence, it is essential to explore the effect of the new current waveform on the rms value. The analysis in this subsection is carried out in the context of the presented control method, i.e. it is generalized for wider range of conversion ratio, considering the operating mode per the status of input and output voltages.

The inductor's current in enhanced-boost and enhanced-buck modes can be divided into three sections. The rms value

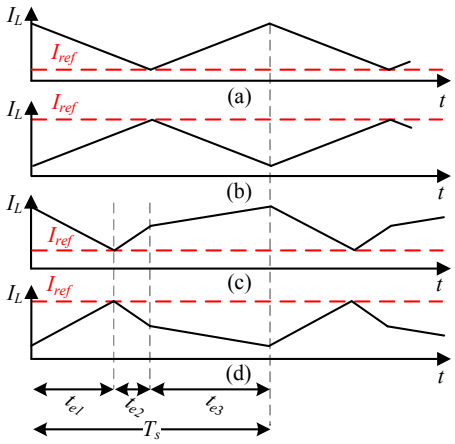

Fig. 4. Inductor current waveforms in various modes (a) conventional-buck (b) conventional-boost (c) enhanced-buck (d) enhanced-boost .

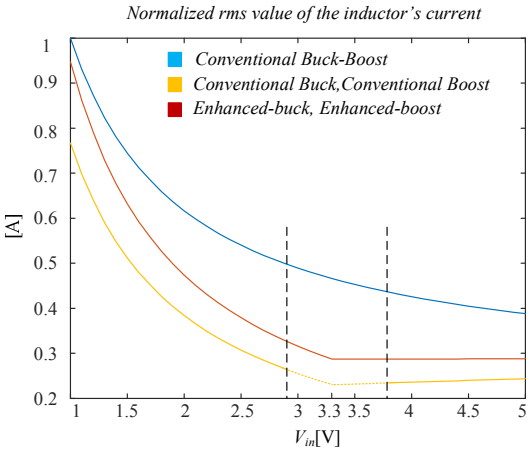

Fig. 5. Normalized rms values of the inductor current under various operating modes.

of the inductor current can be derived using the sum of the squares as:

$$I_{Lrms} = \sqrt{I_{Lrms(1)}^2 + I_{Lrms(2)}^2 + I_{Lrms(3)}^2}\ , \tag{2}$$

where $I_{Lrms(1)}$, $I_{Lrms(2)}$, $I_{Lrms(3)}$ are the rms values of the three parts of the inductor current waveform. The rms value of the inductor's current when operating in conventional buck, conventional boost and conventional buck-boost modes can be expressed as [10]:

$$I_{Lrms\_buck} = \sqrt{I_{out}^2 + (\frac{\Delta I_L}{2\sqrt{3}})^2}\ . \tag{3}$$

$$I_{Lrms\_boost} = \sqrt{\left(\frac{I_{out}}{1-\frac{V_{out}-V_{in}}{V_{out}}}\right)^2 + \left(\frac{\Delta I_L}{2\sqrt{3}}\right)^2}\ . \tag{4}$$

$$I_{Lrms\_buck-boost} = \sqrt{\left(\frac{V_{out}+V_{in}}{V_{in}} I_{out}\right)^2 + \frac{1}{12}\left(\frac{V_{out}V_{in}T_s}{(V_{out}+V_{in})L}\right)^2}\ . \tag{5}$$

To facilitate comparison benchmark, the inductor's current rms value has been normalized with respect to the highest rms value of a conventional buck-boost mode, as can be seen in Fig. 5. The result implies that when feasible, operation in either pure buck or boost is preferred. However, around unity conversion, the new shape for the current as obtained by the enhanced modes, results in lower conduction losses in steady-state compared to conventional approaches.

C. Variable Frequency Operation

To further improve the conversion efficiency, frequency scaling is employed. Operation at high conversion ratio calls for higher frequency operation to lower the ripple efforts and by doing so, reduce the size of the passive components. When operating around unity conversion ratio however, it is possible to lower the operating frequency and by that reduce the switching losses, and more importantly, drive losses. In the enhanced modes, the second time-interval (t_{e2}) with respect to the cycle duration, determines the average value of the inductor current, which is expressed as:

$$I_{L(\text{avg})\_\text{enhanced}-buck} = I_{out}\frac{1}{1-\frac{t_{e2}}{T_s}}\ . \tag{6}$$

$$I_{L(\text{avg})\_\text{enhanced}-boost} = I_{out}\frac{1}{1-\frac{t_{e2}+\frac{V_{out}-V_{in}}{V_{out}}(T_s-t_{e2})}{T_s}}\ . \tag{7}$$

As can be seen from these expressions, keeping the correct ratio between the second interval to the switching period assures that the average current, and hence the load current, are satisfied. This implies that lowering the switching frequency is allowed without jeopardizing the performance, and even improving it. It should be noted however, that a secondary constraint of the maximum allowed ripple sets a lower limit on the frequency. The controller in this study has been designed so that the constraints are met while the switching frequency is adjusted according to the difference (or ratio) between V_{out} and V_{in}.

III. Transient Control

A. Programmable-Deviation Controller

In this section, two recovery patterns are presented within the context of indirect energy transfer conversion (as NIBB) that, compared to the time-optimal solutions, constrain the output voltage deviation or peak inductor current (or both) while maintaining fast convergence in response to load transients. A primary objective in the controller design is to maintain the same hardware for all cases in the steady-state as well as for transients. Therefore, the hybrid controller incorporates the steady-state peak current programmed mode (CPM) arrangement and adds a transient-mode controller. For the transient-mode, two additional logic blocks have been developed, namely the *transient suppression block* and *self-tuning estimator* (see Fig. 1). Upon a load transient detection, these blocks take over the task of estimating the load current and creating the gating signals to the power switches.

The first recovery profile that is described is current-constrained recovery as illustrated in Fig. 6. Upon detection of a loading transient, from I_{old} to I_{ref}, the controller recovers from the loading event in a two-step process. First, the CPM controller is bypassed and Q_1 and Q_4 are turned ON while Q_2 and Q_3 remain OFF, while the new load state is estimated. During this time and based on the new load estimation, the controller sets a threshold for the inductor current, $I_{th}=I_{ref}$. Once the inductor current reaches the assigned threshold, the controller moves along the boundary $I_L=I_{th}$ in a sliding mode operation, causing the output voltage to rise up without changing the inductor current. The definition of the controller and its realization is quite simple and features simple current comparison with some hysteresis band. As a sliding controller, it can be defined as follows:

$$\begin{aligned} &\sigma_i(v_C,i_L)=i_L-I_{ref}, \text{ for } v_C<V_{ref} \\ &on:\ \sigma_i<0 \quad off:\ \sigma i>0 \end{aligned} . \tag{8}$$

The second recovery profile applies constrains on both the output voltage to a desired level and on the inductor current, here the new steady-state value has been assigned. The recovery is described through a three-step process and is illustrated in Fig. 7. First, in a similar way as in the previous mode, the inductor current is ramped up, while the controller sets two thresholds: one for the output voltage and one for the inductor current based on the load estimation. In the second step, the controller is assisted by the voltage threshold to operate as a sliding-mode controller that is defined by

$$\begin{aligned} &\sigma_v(v_C,i_L)=v_C-V_{th}, \text{ for } i_L<I_{th} \\ &on:\ \sigma_v>0 \quad off:\ \sigma_v<0 \end{aligned} . \tag{9}$$

During this step, the inductor current rises without changing the output voltage until it reaches the current threshold and the controller moves to the third step. During the third and final step, the controller moves along the boundary $i_L=I_{th}$ in a sliding mode operation, this can expressed as:

$$\begin{aligned} &\sigma_i(v_C,i_L)=iL-I_{th}, \text{ for } v_C<V_{ref} \\ &on:\ \sigma_i<0 \quad off:\ \sigma_i>0 \end{aligned} . \tag{10}$$

Optimized boundary control scheme covering the entire range of conversion ratios has been designed based on the above-mentioned recovery profiles for loading events and conventional time-optimal solutions for unloading events. The design approach is aided by the analytical derivation of the converter's state trajectories and load-line combined with graphical illustrations of the state-plane for various voltage gains.

The controller recovery pattern for loading events in enhanced-buck mode is an example of exploiting the topological flexibility of the NIBB converter to further improve the transient response while reducing output voltage deviation as well as lowering the peak inductor current that is required for recovering to the new steady-state. Illustrations of the state-plane as well as the specific recovery trajectories for loading transient, in enhanced-buck mode are depicted in Fig. 8. The two constrained recovery profiles (Fig. 8b-c) presented earlier in this section are compared with time-optimal pattern (Fig. 8a) as a benchmark case. It can be seen that while a conventional buck time-optimal recovery ramps the inductor current up by with a slope of $(v_{in}-v_{out})/L \approx 0$, here the the addition of a boosting phase ramps up the inductor current with a slope of v_{in}/L. This improvement alone significantly enhances the recovery performance on both deviation and time properties since it effectively doubles the applied voltage on the inductor. In a similar manner, recovery of enhanced-boost mode for the NIBB converter is found to superior over the one of a conventional boost. This has been widely detailed in [15].

To demonstrate the operation of the transient recovery pattern, simulation testbench (in PSIM) has been constructed. Fig. 9 shows the resultant recovery pattern for 0.8A to 3.5A loading transient, while the converter operated in enhanced-buck mode (3.8V to 3.3V). Fig. 9 depicts the time waveforms for the output voltage and inductor's current as well as the state-plane for better visualization of the trajectories along the recovery phase. It can be seen that the current is well confined within the hysteresis margins during the convergence. It can also be seen that resumption to steady-state is obtained smoothly without additional oscillations due to the correct estimation of the load status (location marked on the timing diagram).

Fig. 10 shows the resultant recovery pattern for a 3.5A to 0.8A unloading transient, while the converter operates in enhanced-buck mode (3.8V to 3.3V). Here, fast convergence is assured by employing conventional time-optimal recovery pattern. Fig. 10 depicts the time waveforms for the output voltage and inductor's current as well as the state-plane representation.

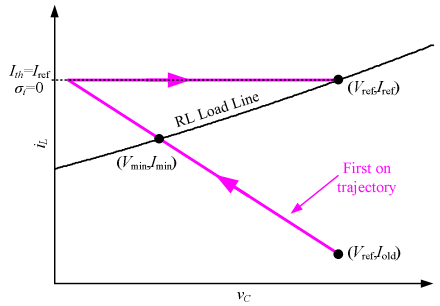

Fig. 6. Illustrative movement of the state plane for the current-constrained mode handling a loading transient.

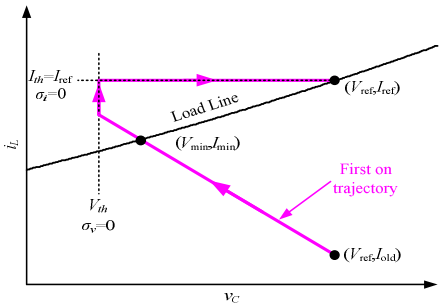

Fig. 7. Illustrative movement of the state plane for the voltage-deviation and current-constrained mode handling a loading transient.

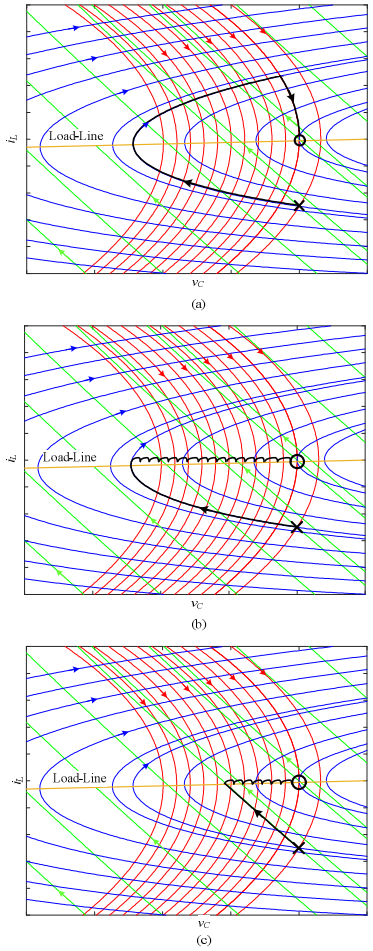

Fig. 9. State plane representation of NIBB operating in enhanced-buck mode for a loading transient. (a) Recovery pattern of conventional Time-Optimal Control (TOC). (b) Recovery pattern of current-constrained mode in conventional buck mode. (c) Recovery pattern of current-constrained mode in enhanced-buck mode with a boost-phase.

IV. PRATICAL IMPLEMENTATION

A. Load Current Estimation

The implementation of the self-tuning estimator is described in Fig. 11. It is based on a look-up-table (LUT) and on estimation of the load current through a comparison with a measurement of the known current value, named unity current. The LUT of the estimator is populated during the converter start-up. Over that period, the LUT's entries are stored, i.e. current and voltage threshold values are created, from measurement of the output voltage. After the writing of the values in the tables is completed, the output voltage deviation is used as an address (input of Fig. 11) to determine the LUT's outputs, i.e., V_{th} and I_{th} values. Upon the converter power up a generic LUT is assigned. The known current of the protective resistor R_{bld} (also known as bleeding resistor), named unit current I_{unit}, is used for the system calibration. During this time, the load is disconnected from the output of the converter, i.e., switch M_{out} is turned off, and in addition, switches Q_1, Q_3 are off while Q_2, Q_4 are on. This assures that the current path to

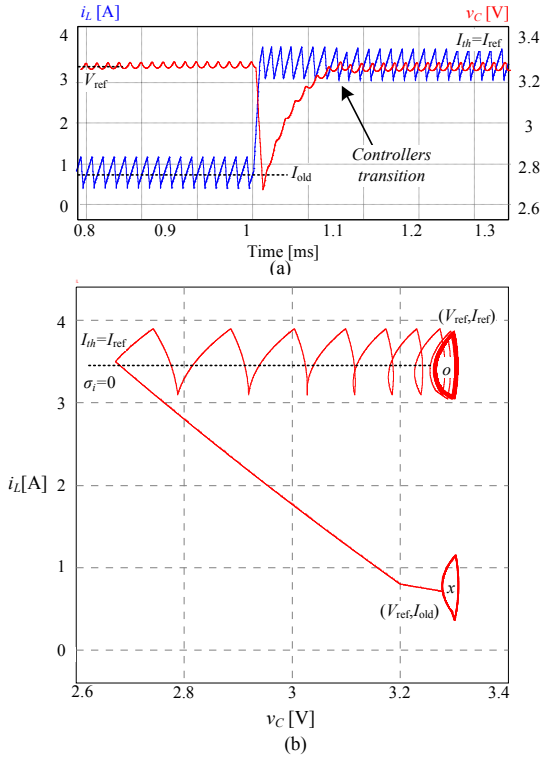

Fig. 9. Simulated response of the current-constrained controller to a 0.8-3.5 A loading transient ot a NIBB converter in enhanced-buck mode. (a) Inductor current (blue) and output voltage (red) (b). State-plane representation of the output voltage and inductor current.

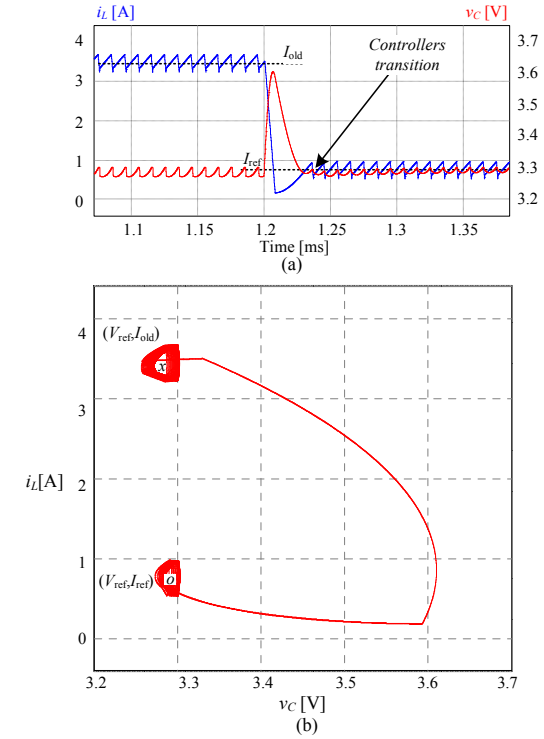

Fig. 10. Simulated result of time-optimal controller to a 3.5A to 0.8A unloading event of a NIBB converter operating in enhanced-buck mode. (a) Inductor current (blue) and output voltage (red). (b) State-plane representation of the output voltage and inductor current.

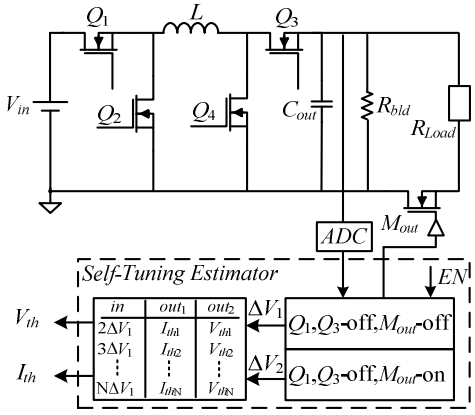

Fig. 11. Block diagram of the self-tuning estimator.

R_{bld} is via the output capacitor alone. The value ΔV_1 is a function of I_{unit} and is measured as:

$$\Delta V_1 = v_{ADC}[n] - v_{ADC}[n-1] = \frac{V_{ref}}{R_{bld}}\frac{\Delta t}{C} = I_{unit}\frac{\Delta t}{C}, \qquad (11)$$

where Δt is the sampling interval, $v_{ADC}[n]$ is the current value of the ADC output and $v_{ADC}[n-1]$ is the ADC value from the previous sampling cycle. The value ΔV_1 is used to populate the LUT with I_{th} and V_{th} values for the full range of allowable output voltage deviations.

Upon power up of the converter and population of the LUT is completed, the switch M_{out}, usually existing in the applications of interest is turned on. During the remaining portion of the converter operation, the LUT is used to produce I_{th} and V_{th} during transient events. The input to the LUT is now the voltage deviation ΔV_2 measured during the on time of Q_1 and Q_4. During a transient event, the load current I_{out}_new is estimated as:

$$I_{out\_new} = \frac{\Delta V_2 - \Delta V_1}{\Delta V_1} I_{unit}. \qquad (12)$$

V. Experimental Verification

In order to validate the operation of the unified current-programmed digital controller, a 2-15V to 3.3V non-inverting buck-boost prototype has been built and tested, using an 8.2μH inductor, 30μF output capacitance and operating frequency of 100-200 KHz. The converter is digitally controlled by a steady-state voltage-mode compensator and a transient-mode controller as shown in Fig 1. The digital controller has been entirely realized on Altera Cyclone IV FPGA , and the total number of logic elements used is 980 for the entire controller.

Steady-state operation has been verified through multiple experiments under various input voltages, as shown in Fig. 12-Fig. 14. Fig. 12a and Fig. 12b show the inductor's current in enhanced-boost mode for V_{in}=2.8V and V_{in}=3.2V, respectively. Regulated output voltage is achieved for a wide range of input voltages while significantly reducing average inductor current and rms values. Fig. 13a and Fig. 13b depict the operation in enhanced-buck mode for V_{in}=3.8V and V_{in}=3.4V, respectively.

Fig. 14 shows a transition mode between conventional boost to enhanced-boost. It can be seen that, seamless transition between the two operating modes is achieved as in all other mode transition cases. A zoomed-in view of the

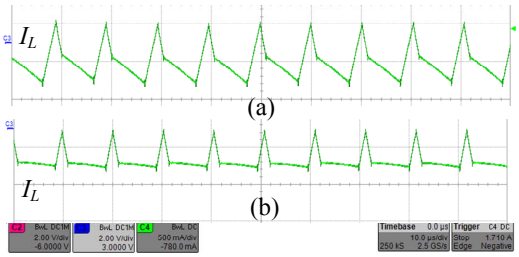

Fig. 12. Enhanced-boost mode, V_{out}=3.3V (a) V_{in}=2.8V (b) V_{in}=3.2V.

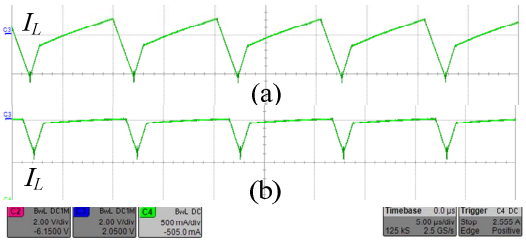

Fig. 13. Enhanced-buck mode, V_{out}=3.3V. (a) V_{in}=3.8V(b) V_{in}=3.4.

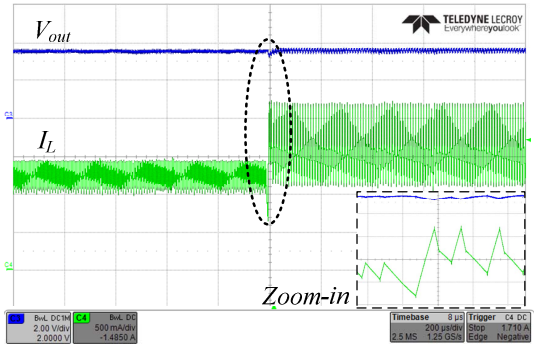

Fig. 14. Transition event from conventional boost to enhanced-boost operating mode, V_{in}=3V, V_{out}=3.3V.

inductor current and output voltage is shown in Fig. 14 demonstrating frequency scaling operation.

The transient controller performance for loading transient of 0.8-3.5A is depicted in Fig. 15-16. Fig. 15 shows the loading transient recovery of the current-constrained controller while in enhanced-buck mode. I_{th} is chosen to be equal to the new steady-state peak inductor current which results in an output voltage deviation of 1V and total transient time of 60μs with no current overshoot. Fig. 16 shows loading transient recovery of the voltage-deviation-and-current-constrained controller while operating in pure-boost mode. The resultant recovery parameters are output voltage deviation of 1V, no current overshoot, recovery time to steady-state is 50μs.

VI. Conclusion

A unified current programmed digital controller for NIBB converter have been presented in this study. The controller incorporate a steady-state CPM controller for steady-state operation and a nonlinear transient-mode controller for load transients. Detailed analysis of the enhanced-modes has been carried out, followed by steady-state control scheme design to allow seamless transition between modes and improved ripple characteristics. Load transients are supported by the same hardware of the CPM controller, with programmable constraints of the output voltage deviation and inductor current.

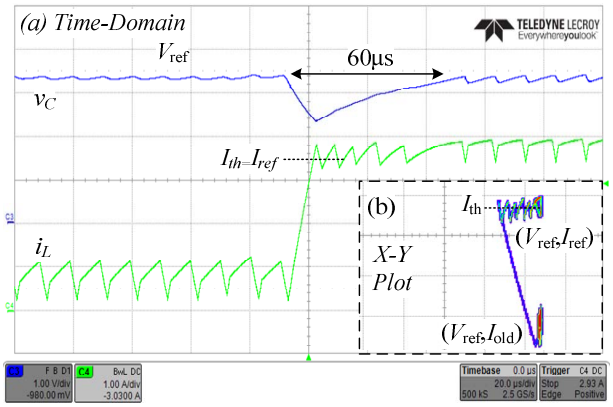

Fig. 15. NIBB converter's response and state-plane representation to a 0.8-3.5 A loading transient using the current-constrained controller. (a) Output voltage (top-blue) 1V/div, inductor current (bottom-green) 1A/div, time scale 20μs/div. (b) State-plane representation of inductor current (vertical axis – 1 A/div) and output voltage (horizontal axis - 1 V/div).

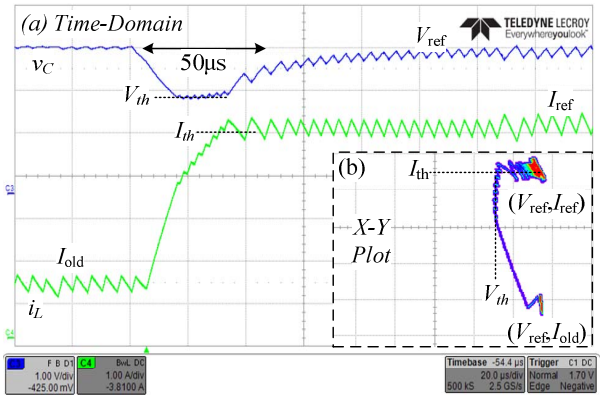

Fig. 16. NIBB converter's response and state plane representation to a 0.8-3.5 A loading transient using the voltage-deviation and current-constrained controller. (a) Output voltage (top-blue) 1V/div, inductor current (bottom-green) 1A/div, time scale 20μs/div. (b) State-plane representation of the inductor current (vertical axis – 1A/div) and output voltage (horizontal axis – 1A/div).

An optimized boundary control scheme for efficient load transient convergence has been perused with assured large-signal stability.

Experimental results of a 2-15V to 3.3V NIBB converter prototype are provided. For steady-state operation around unity conversation, well regulated output voltage is achieved with significantly reduced average inductor current and rms values. The controller exploits the versatile structure of the NIBB to maintain short transient time without the penalty of increased current or voltage overshoots.

REFERENCES

[1] O. Erdinc, B. Vural and M. Uzunoglu, "A dynamic lithium-ion battery model considering the effects of temperature and capacity fading," *International Conference on Clean Electrical Power*, Capri, 2009, pp. 383-386.

[2] B. Sahu and G.A. Rincon-Mora, "A low voltage, dynamic, non-inverting, synchronous buck-boost converter for portable application," *IEEE Transactions on Power Electronics*, vol. 19, pp.443-452, 2004.

[3] C. Yao, X. Ruan, W. Cao and P. Chen, "A Two-Mode Control Scheme With Input Voltage Feed-Forward for the Two-Switch Buck-Boost DC–DC Converter," *IEEE Transactions on Power Electronics*, vol. 29, no. 4, pp. 2037-2048, April 2014.

[4] C. H. Tsai, Y. S. Tsai and H. C. Liu, "A Stable Mode-Transition Technique for a Digitally Controlled Non-Inverting Buck–Boost DC–DC Converter," in *IEEE Transactions on Industrial Electronics*, vol. 62, no. 1, pp. 475-483, Jan. 2015.

[5] J. Ma, M. Zhu, X. Li and X. Cai, "Bumpless transfer of non-inverting buck boost converter among multiple working modes," *2018 IEEE Applied Power Electronics Conference and Exposition (APEC)*, San Antonio, TX, 2018, pp. 1909-1914.

[6] S. M. Ahsanuzzaman, J. Blackman, M. M. Peretz and A. Prodić, "Power management architecture for universal input Ac-Dc adapter support in battery powered applications," *2013 15th European Conference on Power Electronics and Applications (EPE)*, Lille, 2013, pp. 1-9.

[7] A. Babazadeh and D. Maksimovic, "Hybrid Digital Adaptive Control for Fast Transient Response in Synchronous Buck DC–DC Converters," in *IEEE Transactions on Power Electronics*, vol. 24, no. 11, pp. 2625-2638, Nov. 2009.

[8] A. Babazadeh, L. Corradini and D. Maksimovic, "Near time-optimal transient response in DC-DC buck converters taking into account the inductor current limit," *2009 IEEE Energy Conversion Congress and Exposition*, San Jose, CA, 2009, pp. 3328-3335.

[9] Y. Zhang, I. Radović, S.M, Ahsanuzzaman, A. Prodić, G. Calabrese, G. Frattini, M. Granato ., "Low-frequency ripple-shaping controller for operation of non-inverting buck-boost converters near step-up step-down boundary," *2018 IEEE Applied Power Electronics Conference and Exposition (APEC)*, San Antonio, TX, 2018, pp. 292-297.

[10] N. Zhang, S. Batternally, K. C. Lim, K. W. See and F. Han, "Analysis of the non-inverting buck-boost converter with four-mode control method," *IECON 2017 - 43rd Annual Conference of the IEEE Industrial Electronics Society*, Beijing, 2017, pp. 876-881.

[11] J. Ma, M. Zhu, Guanghui Li, Xiuyi Li and X. Cai, "Concept of unified mode control for non-inverting Buck-Boost converter," *2017 IEEE 3rd International Future Energy Electronics Conference and ECCE Asia (IFEEC 2017 - ECCE Asia)*, Kaohsiung, 2017, pp. 1235-1240.

[12] M. M. Peretz, B. Mahdavikhah and A. Prodić, "Hardware-Efficient Programmable-Deviation Controller for Indirect Energy Transfer DC–DC Converters," in *IEEE Transactions on Power Electronics*, vol. 30, no. 6, pp. 3376-3388, June 2015.

[13] G. G. Oggier, M. Ordonez, J. M. Galvez and F. Luchino, "Fast Transient Boundary Control and Steady-State Operation of the Dual Active Bridge Converter Using the Natural Switching Surface," in *IEEE Transactions on Power Electronics*, vol. 29, no. 2, pp. 946-957, Feb. 2014..

[14] V. Yousefzadeh, A. Babazadeh, B. Ramachandran, E. Alarcon, L. Pao and D. Maksimovic, "Proximate Time-Optimal Digital Control for Synchronous Buck DC–DC Converters," in *IEEE Transactions on Power Electronics*, vol. 23, no. 4, pp. 2018-2026, July 2008.

[15] O. Kirshenboim and M. M. Peretz, "Fast Response of Deviation-Constrained Hybrid Controllers for Indirect Energy Transfer Converters," in *IEEE Transactions on Power Electronics*, vol. 33, no. 3, pp. 2615-2629, March 2018.

[16] J. Ma, M. Zhu, G. He and X. Cai, "Breaking performance limit of asynchronous control for non-inverting buck boost converter," *IECON 2017 - 43rd Annual Conference of the IEEE Industrial Electronics Society*, Beijing, 2017, pp. 928-933.

[17] D. C. Jones and R. W. Erickson, "Buck-Boost Converter Efficiency Maximization via a Nonlinear Digital Control Mapping for Adaptive Effective Switching Frequency," *IEEE Journal of Emerging and Selected Topics in Power Electronics*, vol. 1, no. 3, pp. 153-165, Sept. 2013.

[18] X. Hu and P. K. T. Mok, "Analysis and design of three-state controlled transition mode for a buck-boost converter with efficiency and stability enhancement," *2013 IEEE International Symposium on Circuits and Systems (ISCAS2013)*, Beijing, 2013, pp. 697-700.

[19] E. Abramov, T. Vekslender, O. Kirshenboim and M. M. Peretz, "Fully Integrated Digital Average Current-Mode Control Voltage Regulator Module IC," in *IEEE Journal of Emerging and Selected Topics in Power Electronics*, vol. 6, no. 2, pp. 485-499, June 2018.

[20] T. Vekslender, E. Abramov, O. Kirshenboim and M. M. Peretz, "Hardware efficient digital auto-tuning average current-mode controller," *2017 IEEE 18th Workshop on Control and Modeling for Power Electronics (COMPEL)*, Stanford, CA, 2017, pp. 1-8.